Chapter 3
Advanced Surface Characterization Techniques in Nano- and Biomaterials

Ricardo A. Zamora, Cristián Gutiérrez-Cerón, Jesum Alves Fernandes and Gabriel Abarca

Abstract Although metallic nanoparticles have been applied in various fields of biomedical engineering research for quite some time, generating new biomaterials with improved regenerative capabilities remains the cornerstone in tissue engineering and regenerative medicine. These materials, once implanted in patients, will ultimately be invaded by endogenous cells, which emphasizes the relevance of surface composition as a critical factor in determining the regenerative potency of a given material. In this chapter, we present a brief revision on fundamental concepts and an up-to-date overview for surface characterization of nano-engineered structures.

3.1 Introduction

Metal nanoparticles and functionalized metal nanoparticles, bimetallic nanoparticles containing metals such as copper, nickel, silver, and gold, and non-metallic nanomaterials have been widely used in diagnosis and therapeutics [1, 2]. The use of nanomaterials in biomedical applications explodes the nanometric sizes of such materials that confer unique physical and chemical properties. There are several ways to determine the average size of a particle in solution [3, 4]. When a light beam reaches a solution or colloidal dispersion, part of the incident radiation may be absorbed, a part is scattered, and the rest is transmitted through the solution [5]. The intensity, polarization, and angular distribution of the light scattered by a colloidal dispersion depend on the size and shape of the particles, the interactions among them, and the difference between the refractive indexes of the particles and the medium [6, 7]. Light scattering measurements have gained relevance in determining the size, shape, and interactions between the particles [8, 9].

R. A. Zamora · C. Gutiérrez-Cerón
Facultad de Química y Biología, Universidad de Santiago de Chile, Santiago, Chile

J. A. Fernandes
School of Chemistry, University of Nottingham, University Park, Nottingham NG7 2RD, UK

G. Abarca (✉)
Facultad de Ciencias, Centro de Nanotecnología Aplicada, Universidad Mayor, Santiago, Chile
e-mail: gabriel.abarca@umayor.cl

E. I. Alarcon and M. Ahumada (eds.), *Nanoengineering Materials for Biomedical Uses*,
https://doi.org/10.1007/978-3-030-31261-9_3

Dynamic light scattering (DLS), small angle X-ray scattering (SAXS), and small angle neutron scattering (SANS) are the most used analytical techniques based on scattering at small angles of the incident radiation [10, 11]. Such dispersion, regardless of their nature, produces a dispersion pattern, which contains structural information of the sample [9, 12]. Whether we talk about visible light scattering (DLS) or X-ray/neutrons (SAXS and SANS, respectively), we must consider that these types of radiation have two main ways of interacting with matter: absorption and scattering [13, 14]. The dispersion can occur with or without the loss of energy, which leads to the generation of scattering waves with different wavelength (i.e., Compton scattering, inelastic scattering) when there is energy transfer or equal wavelength (Rayleigh scattering and Thomson scattering, elastic scattering) than the incident beam when there is no energy transfer [15].

Rayleigh scattering (visible light) and Thomson scattering (X-ray and neutrons) are generated when the incident radiation collides with the electrons without transferring energy [16]. This interaction produces coherent waves and an interference phenomenon, which allows these to be recorded by a detector. The diffraction pattern obtained allows the obtaining of structural information of the material from these waves.

3.2 Small-Angle X-ray Scattering (SAXS) and Small-Angle Neutron Scattering (SANS)

The SAXS and SANS are analytical techniques based on Thomson scattering that allows the structural characterization of nanomaterials in the range of 1–100 nm (nano to mesoscale) [17]. There are other scattering techniques for materials less than 1 nm (ultra-small-angle X-ray scattering, USAXS) and greater than 100 nm (wide-angle X-ray scattering, WAXS) [12, 18].

SAXS uses X-ray with wavelengths of 0.1–0.2 nm and allows characterizing the size, shape, and morphology of synthetic and natural polymers, nanoparticles, and biomaterials, while SANS technique uses neutrons with a wavelength of 0.5 nm approximately and is widely used to study the size and structural dynamics of nanomaterials [12, 17]. Figure 3.1 top shows the fundamental setup of a SAXS and SANS experiment.

When the SAXS and SANS experiments are performed, the data that is recorded by a detector. The detector records a scattering vector (q), which is defined by subtraction of the scattering wave vector (k_1) and scattering wave incident (k_0). The q vector presents elastic scattering, and the modulus of the scattered wave k_1 is equal to k_0. The q vector is represented mathematically by the expression:

$$q(\lambda, \theta) = (4\pi/\lambda)\sin(\theta) \tag{3.1}$$

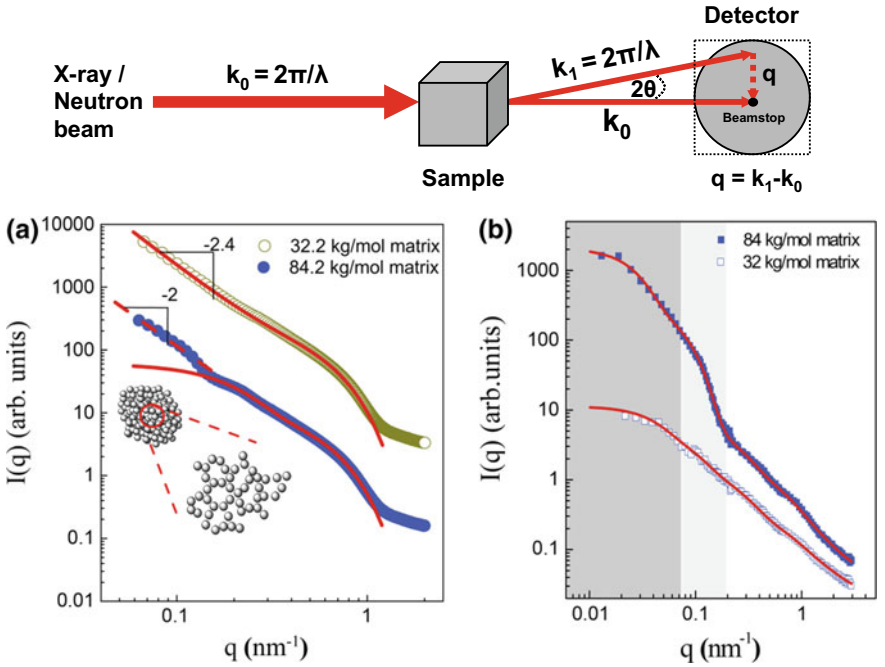

Fig. 3.1 (Top) SAXS and SANS standard setup. (Bottom) PS-grafted Fe_3O_4 nanoparticles measurements profiles, **a** SAXS **b** SANS bottom plots. Reproduced with permission from [19]

The intensity of scattering $I(q)$ is expressed as a function of the scattered vector, which depends on the wavelength (λ) of the incident beam and scattering angle (2θ). The intensity of scattering also is given by (3.2).

$$I(q) = NP(q)S(q) = \Phi \Delta p^2 V P(q)S(q) \tag{3.2}$$

Here, N is the number of particles that scatter the incident beam and the terms $P(q)$ and $S(q)$ represent the form factor and the structure factor, respectively [20]. The form factor is related to the size and shape of the object, and the structure factor is related to the distribution of distances between a particle and its neighbors, being this term an index of the state of aggregation of the sample.

$$P(q) = |\int (\rho(r) - \rho_S)\exp(iqr)\mathrm{d}r|^2 \tag{3.3}$$

For a monodisperse system containing spherical particles, the form factor $P(q)$ can be described by (3.4):

$$P(q) = (\rho - \rho_S)^2 V^2 \left(\frac{3J_1(qR)}{qR}\right) \tag{3.4}$$

If we consider spherical particle having core–shell structure,

$$P(q) = \left[(\rho 1 - \rho 2) V 1 \frac{3J_1(qR_1)}{qR_1} + (\rho 2 - \rho \mathrm{S}) V (3J1qRqR) \right]^2 \tag{3.5}$$

For an isotropic system, the structure factor $S(q)$ can be described by (3.6),

$$S(q) = 1 + 4\pi n \int (g(r) - 1)(\sin qR)/qRr^2 \mathrm{d}r \tag{3.6}$$

where $g(r)$ is the radial distribution function; the above expression depends on the relative position of the particles. For a diluted system, $S(q) \sim 1$.

In practice, the scattering spectrums of SAXS or SANS obtained of the irradiation of samples diluted and monodisperses can be divided into three parts: low-q region, intermediary-q region, and high-q region. The low-q region (the so-called Guinier region) is the region to minimal scattering angles. The analysis of this region allows obtaining for diluted and monodisperse solutions parameters such as radius of gyration (R_g) and the molecular weight (M_w). M_w of the nanoparticles can be obtained by extrapolation of absolute data to $I(0)$, while the R_g is obtained from the expression,

$$I(q) = I(0) \exp\left(R_\mathrm{g}^2 q^2 / 3 \right) \tag{3.7}$$

where the R_g is obtained from the slope ($-R_\mathrm{g}^2/3$) from plot Ln $I(q)$ v/s q^2. The above expression is valid for any particle shapes [18]. When it is known that the shape of the nanoparticles is too elongated or flattened, similar expressions can be used to obtain the corresponding radius [18]. In the intermediary-q region (the so-called Fourier region), the pair distance distribution function can be determined. This phenomenon is possible by an indirect Fourier transformation of the experimental form factor. The calculation of this parameter gives us relevant information about the general shape of the nanoparticle [21].

$$p(r) = 1/2\pi r^2 \int_0^\infty q P(q) \sin(qr) \mathrm{d}r \tag{3.8}$$

The high-q region (the so-called Porod region) is the region at large scattering angles. The data from this region is used to establish characteristics of the surface of the nanoparticle, such as the surface-to-volume ratio and specific surface estimation for small particles [21]. For this, it is necessary to obtain the so-called invariant Q. The invariant Q is obtained by integrating the expression $I(q)q^2$.

$$Q = \int_0^\infty I(q) q^2 \tag{3.9}$$

The integration gives the value of invariant Q, which only depends on the volume of the nanoparticle and not on its shape [17]. Additionally, with the invariant Q, it is possible to obtain the Porod volume, which is generally 1.5 or 2 times the M_w of the nanoparticle [22]. Along with this, if the Guinier approximation is used to extrapolate the value of $I(0)$, it is possible to calculate, along with the invariant Q, the M_w of the nanoparticle according to the expression $M_w = I(0)/Q$.

In addition to the Guinier and Porod approximations, there are other methods to analyze samples of monodisperse and diluted nanoparticles. Among the simplest practices described to perform parameter analysis from SAXS and SANS experiments, we can mention the average size determination method (ADM) [23]. This method is exclusively used for the determination of the size distribution and the shape of particles in monodisperse systems and can be used with a model-free approximation or considering the use of one. In more complex cases, in which the particle system is polydispersed, we can mention as methods of analysis the parametric distribution models (PDM), integral transform methods (ITM), and numerical methods (NM) [23].

The parametric distribution models are the most straightforward methods used to determine the size distribution in polydispersed nanoparticle systems. This method assumes a parametric distribution of the size distribution, while the integral transform methods and numerical methods assume a specific original form. Because the SAXS and SANS techniques are highly specific in determining the distribution of sizes and shapes of different types of nanoparticles, their use as characterization techniques has increased sharply in recent years in scientific journals that have as scope the application of nanoparticles in the biomedical area [24, 25].

3.3 SAXS, SANS, and Its Application in Biomedicine

3.3.1 Tailored Nanoparticles with Antiviral and Antibacterial Activities

The use of nanoparticles as therapeutic agents for the control of various viruses and pathogenic bacteria has taken high relevance in recent years due to the wide variety of materials that can be used for their synthesis [26, 27]. Besides, most nanoparticles are easy to synthesize and present a high ductility in the modification of surface physicochemical properties, along with not being cytotoxic against normal mammalian cells [28]. Currently, many reports show the use of functionalized nanoparticles as antiviral and antibacterial properties [29, 30]. Nanostructures with antiviral activity must have a specific size to be able to reversibly interfere with the virus–cell receptor interaction (virustatic nanoparticles) [31]. Another type of antiviral nanoparticles is the so-called virucidal nanoparticles, which acts irreversibly deactivating the action of the virus [31]. One of the nanoparticles used for this purpose is the mesoporous silica nanoparticles ($mSiO_2$). Silva et al. established for the first time that the $mSiO_2$

nanoparticles have virucidal antiviral activity [32]. In their work, they synthesized and characterized $mSiO_2$ nanoparticles by SAXS, which functionalized with diverse chemical groups on the surface to generate virucidal nanoparticles [33]. The use of SAXS allowed establishing that the modification of the surface with different types of substituents did not alter the uniformity of shape of the functionalized $mSiO_2$ nanoparticles compared to non-functionalized ones (both presented a spherical shape with a similar size distribution). Similarly, Sokolowski et al, complementing measures of SAXS and SANS, characterized anionic and cationic SiO_2 nanoparticles [33]. Yi et al. through time-resolved SAXS could establish the mechanism of growth and the kinetics of formation of this $mSiO_2$ nanoparticles, showing how the use of this technique allowed characterizing structural changes during an increase in this type of nanoparticles at the nanometer scale [34].

Other nanoparticles that have shown efficient antiviral activity are silver nanoparticles (AgNPs). Wuithschick et al. using in situ SAXS could synthesize silver nanoparticles and characterize the average radius of these. The use of SAXS allowed them to standardize a method of synthesis of AgNPs with control of the size of these without the use of stabilizers [35].

In the case of nanoparticles with antibacterial activity, the most accepted mechanism of action of how nanoparticles inhibit bacterial proliferation is by their union to the negatively charged cell surface, thus satisfying the denaturation of proteins and causing cell death [36]. AgNPs are recognized for their antibacterial activity [37]. In another work and using SAXS as a characterization technique of size distribution, Wuithschick et al. developed the first selective post-synthesis method of fractionation by the size of AgNPs synthesized in the same batch [35]. The evaluation of the antibacterial activity of the fractions obtained showed that a smaller size of the AgNPs enhances the antibacterial activity.

3.3.2 Nanoparticles and Cancer Therapies

Another biomedical application of nanoparticles has been their use in the detection, diagnosis, and targeted drug delivery of cancer cells [38, 39]. The use of gold nanoparticles (AuNPs) in this field has expanded due mainly to its relatively easy surface functionalization and its high specificity and permeability toward tumor cells [40]. The high specificity and preferential accumulation in tumor cells present in AuNPs and other metallic nanoparticles are strongly dependent on their size [41]. The above is due to the different permeabilization presented by healthy and tumoral tissues [40]. By passive targeting, nanoparticles can enter into tumor cells due to the enhanced permeability and retention (EPR) phenomenon that they present [42]. Le Goas et al. synthesized and characterized AuNPs functionalized with various polymers and copolymers to study their potential use as radiosensitizers in cancer therapy [43]. The AuNPs and functionalized AuNPs were irradiated with multiple doses of gamma rays to evaluate their capacity to generate reactive species against tumor cells. Complementing measures of SAXS and SANS, they were able to fully characterize

the effect of gamma irradiation on the structures of these nanoparticles [43]. SAXS measurements showed that the metal core of the AuNPs did not undergo structural modifications and SANS measurements showed that only the polymer crown of these AuNPs was affected by radiation doses. Other nanoparticles used as cancer treatment and characterized by SAXS and SANS have been the copper nanoparticles (CuNPs) [44, 45] and AgNPs [46].

3.3.3 Proenzyme-like Nanoparticle

A proenzyme is an enzyme temporary inactivated physically or chemically, which upon adequate external stimulus recovers its catalytic activity [47]. One of the few examples of materials with this property for a future biomedical application in biological systems with high oxidative stress is the nanoparticles of $Ce(OH)_3$. Bohn et al. synthesized these nanoparticles and evaluated their catalytic activity against the dismutation reaction of superoxide (O_2^-) to molecular oxygen (O_2) and hydrogen peroxide (H_2O_2) [48]. These nanoparticles acquire superoxide dismutase activity in the presence of H_2O_2. Upon contact with H_2O_2, the content of Ce(III) decreases, the nanoparticles of $Ce(OH)_3$ becoming nanoparticles of the type $CeO_{(2-X)}$ type, which present superoxide dismutase activity. To obtain this type of nanoparticles and that these were stable at physiological pH, an innovative strategy of synthesis was used, which consisted of using phytantriol, amyotrophic liquid crystal [48]. The characterization by SAXS allowed determining the phase structure of the systems. The SAXS curves displayed diffraction peaks, which confirmed that the samples were assembled as a lyotropic liquid crystalline structure. The SAXS results suggested that the nanoparticles were in the aqueous domains of the liquid crystalline systems.

3.4 X-ray Photoelectron Spectroscopy (XPS) and X-ray Absorption Spectroscopy (XAS)

X-ray photoelectron spectroscopy (XPS) is one of the main techniques used in the characterization of the biomaterial surface because of its responsibility for the success or failure of a biomaterial device [49]. In addition to providing a composition, it is possible to verify the chemical environment of the atoms of the sample surface [50]. XPS technique is considered a relatively non-destructive, quite mature method, increasingly used in different areas of biology, including cell, bacteria, and tissue analysis, as well as bioengineering [51]. This susceptible surface technique is frequently being used in the field of biomolecule characterization for application with proteins, peptides, lipids, mucins, enzymes, and DNA [52, 53].

XPS is a technique based on the photoelectric effect, in which the surface to be analyzed is irradiated with soft X-ray photons (conventional sources of Mg Kα

(1253.6 eV) and Al Kα (1486.6 eV), or synchrotron radiation is used whose energy can be chosen within specific intervals) [54]. When a photon of energy $h\nu$ interacts with an electron at a level with binding energy (*BE*), the energy of the photon is entirely transferred to the electron, with the result of the emission of a photoelectron with *KE* (kinetic energy). Figure 3.2 illustrates the photoelectric effect for an isolated atom, where a photoelectron of the electronic layer *K* is emitted [55]. In this context, when the Fermi levels of the sample and the analyzer are leveled, the sample work function (φ) is replaced by the analyzer's work function (φ). An additional work (φ) is required to altogether remove the electron from the material to the so-called vacuum level. In addition, (3.10) indicates that any change in the *BE*s will be reflected in the *KE*s, which means that changes in the chemical environment of an atom can be studied with changes in photoelectronic energies, supplying chemical information. XPS can analyze all the elements of the periodic table except for hydrogen and helium.

The kinetic energy of the photoelectron emitted can be written as:

$$KE = h\nu - BE - \varphi \tag{3.10}$$

where *KE* kinetic energy of the photoelectron; $h\nu$: incident photon energy; *BE*: binding energy; φ: sample work function.

For the analysis of the photoelectrons, hemispherical analyzers are used, which are made up of two metal half-spheres, among which there is a potential difference. The sample should be kept in an ultrahigh vacuum chamber to keep the sample surface unchanged during data collection and to minimize the inelastic scattering [56]. An electric field is generated between the half-beads of the analyzer due to the potential difference applied. This electric field is responsible for selecting the electrons that arrive at the analyzer with specific kinetic energy. At the input of the analyzer, there are electrostatic lenses that have the function of focusing and delaying the photoelectrons up to selected energy, called passing energy because they have kinetic energy values too high to be deflected in the path inside the analyzer. At the end of the electron trajectory, there is a multichannel detector, where each channel is

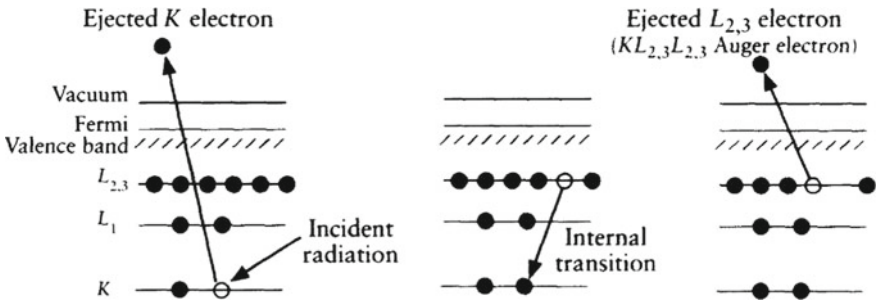

Fig. 3.2 Representation of the photoelectron emission process and Auger effect. Reproduced with permission from [55]

responsible for a range of energy. Thus, each electron detected in a specific energy interval adds a count in the channel. Hence, the photoemission spectrum is obtained as a function of kinetic energy (Fig. 3.2).

The primary information obtained in XPS measurements is the composition and the chemical state of the atoms on the surface of the samples [56]. The intensity of a given peak in the photoemission spectrum is proportional to the concentration of corresponding atoms in the sample [57]. The XPS spectrum is formed by a series of peaks, on a background, produced by the inelastic collisions of the electrons that lose most of their energy before leaving the sample. The energy of the X-rays used limits the electronic levels of each element that can undergo photoionization, so they only photoemit the levels with the highest useful absorption section of the incident photons. For each chemical element, a set of peaks is always observed at characteristic energies that allow it to be identified, usually using the most intense photoelectronic peak or central peak, to perform the quantitative and chemical state analysis. In addition to this type of peaks, others may appear due to other processes (Auger peaks), making the XPS spectrum sometimes complicated (Fig. 3.3).

The XPS chemical shift can be described as (3.11):

$$E_b^i = k_{qi} + \sum_j \frac{q_j}{r_{ij}} + E_b^{\text{ref}} \tag{3.11}$$

where E_b^i determine the XPS binding energy, k proportionality constant, q_i charge of the atom, $\sum_j q_j / r_{ij}$ sum of Coulomb contributions from the neighbors at distance r_{ij}, E_b^{ref} reference energy (e.g., metal). The inelastic mean free path corresponds to the average distance that an electron with specific energy can traverse in a sample before it undergoes an inelastic collision [56]. Figure 3.4 shows the dependence of the inelastic mean free path with the kinetic energy of the electrons; this curve is also

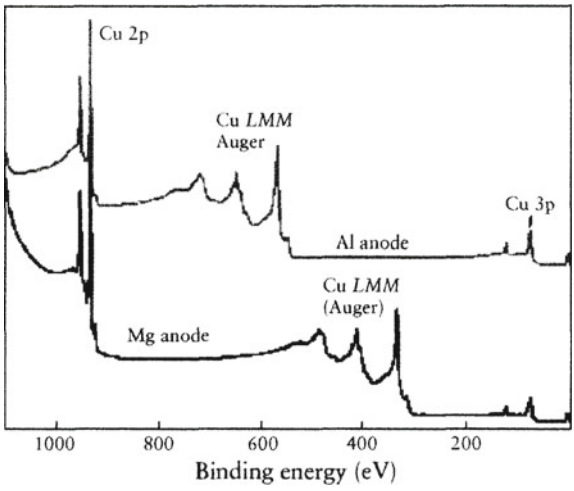

Fig. 3.3 XPS spectrum of a standard copper powder sample acquired by Al Kα and Mg Kα sources to distinguish between XPS and Auger peaks. Reproduced with permission from [55]

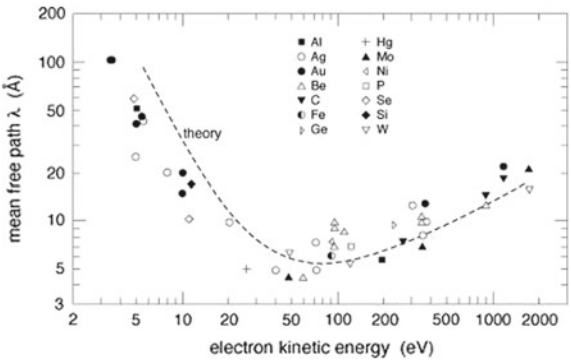

Fig. 3.4 Mean inelastic free path (λ) as a function of the kinetic energy of the electrons for different materials. The continuous curve represents the theoretical prediction, while the points are experimental data for some elements. Reproduced with permission from [58]

known as the universal mean free path curve [55, 56]. The XPS technique is widely used in the characterization of nanometric materials because it has a high sensitivity to the surface of the sample due to the short inelastic free path of the electrons inside the solid.

3.5 XPS for Biomaterial Characterization with Bio-pharm-med Applications

3.5.1 Biomaterial Biocompatibility and Their Use as Drug Delivery

The scientific and technological development in the field of biomedicine seeks to increase the effectiveness of medicines through new designs in their supply or administration systems of active substances. Challenges in drug delivery systems involve the effective localization of therapeutic substances in preselected locations, and in concentrations that maximize their effectiveness [59, 60]. Encapsulation of active materials is widely used today in the medical, pharmaceutical, and cosmetic industries for the development of controlled release delivery systems [59]. Many therapeutically active molecules must be encapsulated in a system that prevents their degradation and guarantees their effective delivery in the corresponding biological medium. Silk fibroin biomaterial-functionalized carbon nanotubes for high water dispersibility were presented by Sun et al. [61]. Multiwalled carbon nanotubes (MWCNTs) functionalized with water-soluble silk fibroin (SF) were prepared via chemical modification, showing low in toxicity. Additionally, a methyl thiazolyl tetrazolium assay was performed to assess biocompatibility, and the results indicated the desirable biocompatible properties of MWCNTs due to SF functionalization (amino-terminated groups). XPS results determine the chemical species introduced by the modification, especially C=O, COOH groups, that help to improve their water dispersibility, transforming MWCNTs in suitable materials for applications in biological and biomedical

systems and devices. In this field, Pawlik et al. reported the use of amorphous TiO_2 (am) layers modified with 3-aminopropyltriethoxysilane (APTES), as drug delivery systems and scaffolds for cell culture [62]. However, the use of NaOH enhanced the ibuprofen release from TiO_2 am layers, improving the metabolic activity of adhered cells compared with the non-modified and NaOH-modified TiO_2 layers (Nam). XPS showed a substantial difference before (TiO_2-am, and Nam) against APTES modification (ANam). The presence of Si 2p and N 1s peaks and a slight increase in the intensity of the C1s peak for the sample modified with APTES, confirming that the two-step modification (NaOH and APTES) procedure was applied effectively [62].

Urothelial diseases (UD) were studied using bilayer swellable drug-eluting ureteric stent (BSDEUS) [63]. This new drug delivery platform technology was applied for the treatment of UD, such as strictures and carcinomas. BSDEUS consists of a stent spray-coated with a polymeric drug containing polylactic acid-co-caprolactone (PLC) layer which is overlaid by a swellable polyethylene glycol diacrylate (PEGDA)-based hydrogel. XPS measurements were performed on the drug-and-PLC-coated stents to evaluate the effect of plasma treatment times on the surface oxidation, indicating an increase in oxygen content at longer plasma duration.

3.5.2 Biomaterials Applied as Antimicrobials and Cancer Agents

Different studies have evaluated the antimicrobial effect of various materials of biological origin; among these, chitosan, a natural polymer, biodegradable, non-toxic in moderate concentrations, and bearer of some antimicrobial activity stands out as one of the most recurrently used materials [64]. The antimicrobial effect of chitosan is attributed to the chelating capacity and the presence of a positively charged amino group that can interact with the compounds of opposite charge and which are present on the surface of the microorganisms [60, 64].

Adjnik et al. examined the physicochemical properties of functionalized silicone materials with antimicrobial coatings and chitosan over the surface [65]. The authors found a strong influence of the use of silicones by drug-embedded chitosan nanoparticles. Furthermore, in vitro drug release testing was used to follow the desorption kinetics and antimicrobial properties were tested by a bacterial cell count reduction assay using the standard gram-positive bacteria *Staphylococcus aureus*. XPS analysis shows that the presence of nitrogen indicates that the chitosan nanoparticles with the incorporated drug were attached to the silicone material, which confirms that they are suitable materials to being studied as an antimicrobial agent. Antimicrobial peptides (AMPs) were analyzed and presented by He et al, using a novel antimicrobial surface by AMPs with improved stability [66]. The authors reported that antimicrobial peptide HHC36 with L-propargylglycine (PraAMP) to improve its salt-tolerant activity and integrate this PraAMP onto the spacer molecule by click chemistry. XPS

confirmed the success of the immobilization, observing that structural changes occurring during the two synthetic processes, which improved the stability, particularly an enhanced enzymolysis tolerance.

Duta et al. studied and demonstrated that the post-deposition thermal treatment of new bioactives, antimicrobial and adherent coatings of nanostructured carbon double-reinforced with silver promotes a higher amorphization and an increase of the sp^2/sp^3 C species ratio [67]. Moreover, no contaminants were detected inside deposited structures. XPS was also applied to determine the structural composition of combinatorial maps fabricated from chitosan and biomimetic apatite powders for orthopedic applications, validating the chemical composition of the C-MAPLE thin films [67]. Accordingly, the survey spectra acquired on the surface of CHT-BmAp samples exhibit: C 1s, O 1s, N 1s, Ca 2s, Ca 2p, P 2s, and P 2p photoelectron peaks. The atomic ratio (N 1s/N 1s + Ca 2p) is decreasing from CHT to BmAp compounds, indicating the composition gradient of combinatorial layers. On the other hand, the Ca 2p/P 2p ratio for CHT-BmAp compounds varied between 0.9 and 1.03 along the sample length [67].

Recently, Fojtu et al. report the synthesis of black phosphorus nanoparticles (BPNPs) and exploration of their applicability in targeted drug delivery [68]. BPNPs are loaded with platinum agents—cisplatin and oxaliplatin and explored the applicability of BP loaded with two commercial platinum anticancer agents, cisplatin (CP) and oxaliplatin (OP). The binding abilities of cisplatin and oxaliplatin to the FLBP surface were examined by wide scan XPS. The peaks from 72.5 to 76.5 eV confirmed the presence of Pt–P bonds in CP- and OP-bound BP. The binding between OP and BP was much stronger than that between CP and BP because of the presence of 1,2-diaminocyclohexane and a new oxalate group in OP. Thus, BP–OP presented higher cytotoxicity when assessed in the human ovarian cancer cell line A2780 after treatment for 24 h. Todea et al. investigated the used XPS to analyze new solid forms of antineoplastic agent 5-fluorouracil (5-FA) with anthelmintic piperazine [69]. The authors emphasized that XPS allows to elucidated information on the atomic environments of 5-FA, where the deconvolution of N 1s core level allows to determine undoubtedly that the protonated (salt) from hydrogen-bonded (co-crystal) nitrogen species [69].

3.6 X-ray Absorption Spectroscopy (XAS)

The X-ray absorption spectroscopy technique allows studying the local atomic structure around an individual atom [70]. This technique has been used in the characterization of nanometric materials to provide electronic information (oxidation state and density of unoccupied states) and structural (interatomic distances, coordination number, and structural disorder) around a specific atom [71]. An essential point in the use of the XAS technique is the possibility of in situ measurements, that is, measurements performed during reactions at different temperatures and with varying atmospheres of gas interacting with the sample.

The use of the XAS technique requires the use of high-brightness, monochromatic radiation with enough energy for each element that is analyzed (chosen by varying the angle of incidence of the polychromatic radiation in a monochromator crystal) [71]. Hence, the synchrotron radiation emitted when charged relativistic particles (usual electrons with energy between 100 MeV and 10 GeV) are deflected by magnetic fields is essential for performing XAS measurements. This radiation covers a wide range of the electromagnetic spectrum, from infrared to hard X-rays. Synchrotron radiation has a brightness thousands of times higher than the radiation produced by conventional X-ray tubes. The XAS technique consists of measuring the absorption coefficient of X-rays as a function of the energy of the incident monochromatic beam. The X-ray absorption coefficient measured in the XAS experiment can be described by the Beer–Lambert Law (3.12):

$$I = I_0 e - \mu x \tag{3.12}$$

where I—transmitted beam intensity; I_0—incident beam intensity; μ—material absorption coefficient; x—sample thickness. When a beam of X-rays of intensity I_0 passes through a material of thickness x, the transmitted beam has its intensity reduced due to various phenomena of X-ray interaction with matter. However, for this energy range of incident radiation, the most important aspect is the absorption of photons through the photoelectric effect. The absorption coefficient presents direct dependence on the energy of the incident X-rays, decreasing with the increase in the energy of the incident photons. It can be observed that in specific energies there is a rapid increase in the coefficient of absorption. The region in energy where this increase occurs is called the absorption edge and is characteristic of each element.

Considering an isolated absorber atom, that is, without any near neighbor atom, the theoretical absorption spectrum after the edge must be a smooth-type drop without oscillations [72]. However, when the absorber atom has several close neighbors (Fig. 3.5), oscillations are observed after the absorption edge. These oscillations occur due to the scattering of the photoelectrons by the atoms neighboring the absorber atom, creating interferences between the backscattered wave function by the neighboring atoms with the wave function emitted by the absorber. The interferences may be constructive or destructive and produce the oscillations observed after the absorption edge.

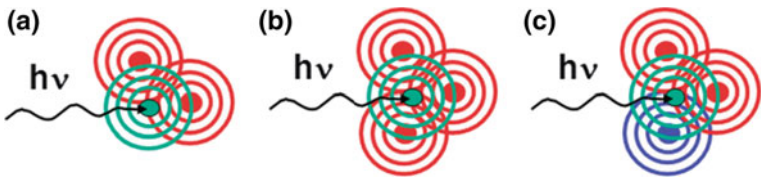

Fig. 3.5 Schematic of the EXAFS effect: The photoelectron ejected from the X-ray absorbing atom is scattered by different configurations of neighbors. Adapted with permission from [72]

The absorption of a photon occurs when the energy of the incident beam ($h\nu$) is greater than or equal to the bonding energy of the electrons (E_b), that is, $h\nu \geq E_b$. When the incident beam has energy $h\nu$ smaller than the bonding energy (E_b) of an electron, or, i.e., $h\nu < E_b$, the emission of photoelectrons of this layer does not occur [72, 73]. However, when the energy of the incident beam is higher than the Eb of the electrons ($h\nu > E_b$), the photoelectron has kinetic energy (E_k) and is scattered by the potential of the neighboring atoms. The photoelectron emitted can be considered as a spherical wave of wavelength (3.13):

$$\lambda = 2\pi k \tag{3.13}$$

where k is the photoelectron wave vector (3.14)

$$k = \frac{2\pi}{h}\sqrt{2m_e E_k} = \frac{2\pi}{h}\sqrt{2m_e(h\upsilon - E_b)} \tag{3.14}$$

$$\chi(k) = \sum_j A j(k) \sin\left(2kr_j + \Phi j(k)\right) \tag{3.15}$$

m is the mass of the electron and $\hbar = h/2\pi$ (h is the Planck constant) [72]. The absorption spectrum is divided into two distinct energy regions, as shown in Fig. 3.6 as follows:

X-ray absorption near edge structure (XANES) involves a range of energy near the absorption edge and up to 50 eV after the edge [72, 74]. In the XANES region, the wavelength of the photoelectron is of the order of the interatomic distances, so the free inelastic mean free path is broad, and multiple scattering occurs before it

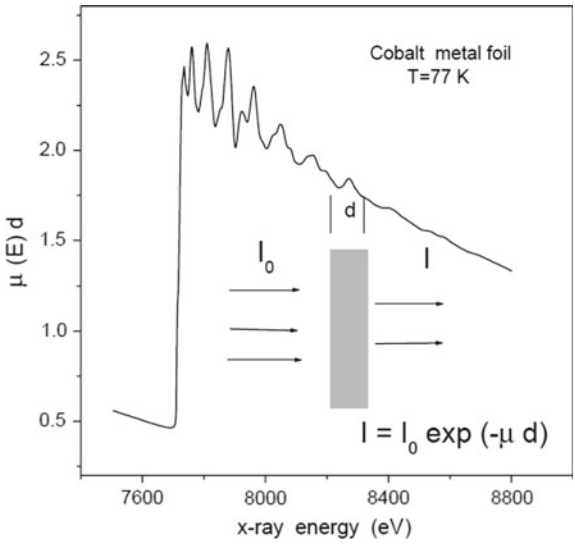

Fig. 3.6 Transmission spectrum at the Co K-edge as a function of the photon energy; d is the thickness of the metal foil; $\mu(E)$ is the absorption coefficient. Reproduced with permission from [74]

returns to the absorptive atom (Fig. 3.6). In addition to the multiple scattering, the XANES region allows transitions to unoccupied levels, so this technique will enable us to obtain information about the oxidation state and the density of empty states of the absorber atom.

The observed oscillations in the EXAFS region depend on the photoelectron wavelength, the number of neighbors, atomic number, and position of the neighboring atoms [75]. These oscillations of the EXAFS χ (k) region can be described as the sum of the contribution from the scattering of the photoelectron in different layers j:

$$A_j(k) = N_j \frac{e^{-2r_j/\lambda(k)}}{kr_j^2} S_0^2(k) F_j(k) e^{-2k^2\sigma_j^2} \tag{3.16}$$

where, N_j—number of atoms present in layer j (coordination numbers); S_0^2—amplitude reduction factor; k—photoelectron wave vector; $F_j(k)$—backscatter amplitude of the photoelectron with wave vector k (chemical sensitivity); σj—Debye–Waller factor; r_j—distance between the scattering atom j and the absorber atom; Φ_j k—phase shift due to scattering, and $\lambda(k)$ inelastic mean free path of the photoelectron [75].

The term $e^{-2r_j/\lambda(k)}$ has a dependence on the inelastic mean free path and represents the attenuation of the wave associated with the photoelectron when it travels through a solid. The exponential $e^{-2k^2\sigma_j^2}$ provides the sample disorder through the Debye–Waller factor, σ_j, which includes contributions of thermal and structural disorder. Factor 2 in the exponentials and in the sine indicates that the photoelectron traverses a closed path between the scattering atom and the absorber. The term $1/r^2$ reflects the fact that the photoelectron ejected from the atom behaves like a spherical wave, where the intensity decreases with the square of the distance. The argument of the sine function depends on k, R, and $\Phi_j k$; the value of $\Phi_j k$ is simulated. The energy loss processes are considered by the amplitude reduction factor S_0^2. The scattering amplitude $F_j(k)$ is the probability of the wave function of the photoelectron with wave vector k being scattered at a given angle by the neighboring atoms. Thus, the analysis of EXAFS oscillations allows the obtaining of structural parameters such as the number of neighboring atoms, Debye–Waller factor, and interatomic distances [72, 75].

3.6.1 XAS for Biomaterial Characterization with Bio-pharm-med Applications

A vast number of reports have been used X-ray absorption spectroscopy to characterize and obtain information about the chemical state and neighborhood of the NPs with strong bio-pharm-med applications [76, 77]. Recently, Rubina et al. reported the use of AgNPs to understand the multifunctional interaction of the system collagen—chitosan material containing silver nanoparticles and non-steroid anti-inflammatory

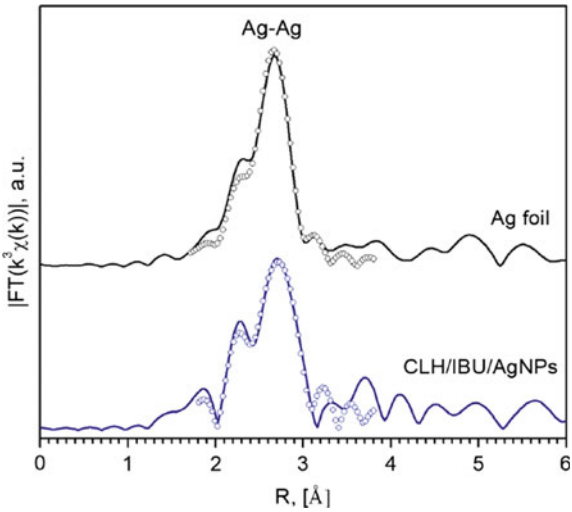

Fig. 3.7 Fourier transforms of EXAFS spectra for CLH/IBU/AgNPs: experimental (line) and best-fit theoretical (open circles) curves. Reproduced with permission from [78]

drug ibuprofen [78]. In this work, they proposed the in vitro release of ibuprofen in phosphate buffer, where the drug release to the solution is governed by Fickian diffusion. The use of AgNPs does not affect the diffusion mechanism, showing that these materials have no specific interactions of AgNPs with a collagen-chitosan scaffold and ibuprofen detected (Fig. 3.7).

Ma et al. examined the atomically dispersed Fe–N_4 sites anchored on N-doped porous carbon materials (Fe-SAs/NC) [78]. These materials can mimic two antioxidative enzymes of catalase and superoxide dismutase and therefore serve as a bifunctional single-atom-based enzyme for scavenging reactive oxygen species (ROS) to remove excess ROS generated during oxidative stress in cells. Using XANES and EXAFS, it was possible to investigate the local structure of Fe-SAs/NC at the atomic level, suggesting that the valence state of Fe in Fe-SAs/NC was between +2 and +3. Also, the obtained coordination number of Fe in the Fe-SAs/CN was about 4, and the bond length between Fe atoms and surrounding coordination atoms (N) was 2.01 Å, corresponding to the first coordination shell of Fe–N.

XANES was also used to describe a multifunctional magnetic drug delivery system made up of iron oxide nanoparticles (IONPs) and a Pluronic F127 shell, to carry doxorubicin (DOX) for neuroblastoma treatment. Mdlovu et al. analyzed to characterize the components of this system, where XANES was performed to understand the fine structure arrangement, electronic configuration, stereochemistry, and oxidation states in terms of bond distance and coordination number of Fe, demonstrated an absorbance feature (Fe = 7112 eV) of a 1s to 3d transition. The 3-(4,5-dimethylthiazol-2-yl)-2,5-diphenyltetrazolium bromide (MTT) results proved that the prepared nanocarriers were non-toxic when tested on *BE*–2–M17 cells [79].

During the last decade, several studies have reported the development of calcium phosphate varieties, scaffolds with random or ordered porosity for anticancer and

antibacterial treatment. Within this family, a new generation of biomaterials with multifunctional europium(III)-doped Hap scaffolds has shown remarkable developments [79]. The luminescent multifunctional biomaterials show potential for use in various biomedical applications such as smart drug delivery, bioimaging, and photothermal therapy [80]. XANES and EXAFS showed that Eu^{+3} ions were incorporated preferentially at the Ca site with local charge compensating via oxygen interstitial ion for samples calcined under air at 450 °C/4 h °C. This effect was due to two possible phenomena: (i) reduction in the average coordination number of Eu(III) ions on the samples produced in the presence of CTAB, or (ii) increase in the Debye–Waller factor that can be associated with an increase in local intrinsic disorder induced by CTAB interaction with cationic Ca^{2+} or PO_4^{3-} ions [81].

3.7 Conclusions and Outlook

In this chapter, a short outline of the theory of SAXS, SANS, XPS, XANES, and EXAFS, with some examples of state-of-the-art experiments and applications were presented. In brief, neutron scattering determines the structure with unique possibilities to understand the atomic distribution at microscopic level and adsorbed molecules in different biomedical applications. XPS offers the possibility to study the surface sense with elemental composition and distribution of oxidation states, with an analytical potential for synthesis and characterization of new biomaterials. Synchrotron-based speciation with XAS offers unique features for the analysis of chemical element species in biological samples. The use of synchrotron radiation measures (XANES, EXAFS) highlighted the importance of the advanced techniques to characterize these new biomaterials, especially under reaction conditions. It is possible to explore the properties of atoms located at the surface or isolated with the aim to understand the behavior under biological conditions.

Acknowledgements The authors are grateful to FONDECYT Iniciación N°11170879. RZB thanks Dicyt-USACH for a postdoctoral grant N021841AL_POSTDOC.

Disclosure All authors have read and approved the final version.

References

1. McNamara K, Tofail SAM. Nanosystems: the use of nanoalloys, metallic, bimetallic, and magnetic nanoparticles in biomedical applications. Phys Chem Chem Phys. 2015;17(42):27981–95.
2. Mout R, Moyano DF, Rana S, Rotello VM. Surface functionalization of nanoparticles for nanomedicine. Chem Soc Rev. 2012;41(7):2539–44.
3. Huang X, Li L, Liu T, Hao N, Liu H, Chen D, Tang F. The shape effect of mesoporous silica nanoparticles on biodistribution, clearance, and biocompatibility in vivo. ACS Nano. 2011;5(7):5390–9.

4. Spicer CD, Jumeaux C, Gupta B, Stevens MM. Peptide and protein nanoparticle conjugates: versatile platforms for biomedical applications. Chem Soc Rev. 2018;47(10):3574–620.
5. Rahman IA, Padavettan V. Synthesis of Silica nanoparticles by Sol-Gel: size-dependent properties, surface modification, and applications in silica-polymer nanocompositesa review. J Nanomater. 2012;2012.
6. Carlson C, Hussein SM, Schrand AM, Braydich-Stolle LK, Hess KL, Jones RL, Schlager JJ. Unique cellular interaction of silver nanoparticles: size-dependent generation of reactive oxygen species. J Phys Chem B. 2008;112(43):13608–19.
7. Woźniak A, Malankowska A, Nowaczyk G, Grześkowiak BF, Tuśnio K, Słomski R, Zaleska-Medynska A, Jurga S. Size and shape-dependent cytotoxicity profile of gold nanoparticles for biomedical applications. J Mater Sci. 2017;28(6):1–11.
8. Alford A, Kozlovskaya V, Kharlampieva E. Small angle scattering for pharmaceutical applications: from drugs to drug delivery systems. In: Chaudhuri B, Muñoz IG, Qian S, Urban VS, editors. Biological small angle scattering: techniques, strategies and tips. Singapore: Springer; 2017. p. 239–62.
9. Li T, Senesi AJ, Lee B. Small angle X-ray scattering for nanoparticle research. Chem Rev. 2016;116(18):11128–80.
10. Di Cola E, Grillo I, Ristori S. Small angle X-ray and neutron scattering: powerful tools for studying the structure of drug-loaded liposomes. Pharmaceutics. 2016;8(2):1–16.
11. Nawroth T, Johnson R, Krebs L, Khoshakhlagh P, Langguth P, Hellmann N, Goerigk G, Boesecke P, Bravin A, Duc GL and others. Target nanoparticles for therapy-SANS and DLS of drug carrier liposomes and polymer nanoparticles. J Phys Conf Ser. 2016;746(1):28–31.
12. Chu B, Liu T. Characterization of nanoparticles by scattering techniques. J Nanopart Res. 2000;2(1):29–41.
13. Becker J. Plasmons as sensors. Berlin, Heidelberg: Springer; 2012.
14. Roe PMSRJ, Roe RJ. Methods of X-ray and neutron scattering in polymer science. New York: Oxford University Press; 2000. p. 331.
15. Kempkens H, Uhlenbusch J. Scattering diagnostics of low-temperature plasmas (Rayleigh scattering, Thomson scattering, CARS). Plasma Sour Sci Technol. 2000;9(4):492–506.
16. In the case of neutrons, these are dispersed by the nucleus.
17. Craievich AF. Small-angle X-ray scattering by nanostructured materials. In: Klein L, Aparicio M, Jitianu A, editors. Handbook of sol-gel science and technology: processing, characterization and applications. Cham: Springer International Publishing; 2018. p. 1185–230.
18. Dmitri IS, Michel HJK. Small-angle scattering studies of biological macromolecules in solution. Rep Prog Phys. 2003;66(10):1735.
19. Jiao Y, Akcora P. Understanding the role of grafted polystyrene chain conformation in assembly of magnetic nanoparticles. Phys Rev E. 2014;90(4):1–9.
20. Bonini M, Fratini E, Baglioni P. SAXS study of chain-like structures formed by magnetic nanoparticles. Mat Sci Eng C. 2007;27(5–8 SPEC. ISS.):1377–81.
21. Boldon L, Laliberte F, Liu L. Review of the fundamental theories behind small angle X-ray scattering, molecular dynamics simulations, and relevant integrated application. Nano Rev. 2015;6(1):25661.
22. Londoño OM, Tancredi P, Rivas P, Muraca D, Socolovsky LM, Knobel M. Small-angle X-ray scattering to analyze the morphological properties of nanoparticulated systems. Cham: Springer International Publishing; 2018. p. 37–75.
23. Agbabiaka A, Wiltfong M, Park C. Small angle X-ray scattering technique for the particle size distribution of nonporous nanoparticles. J Nanoparticles. 2013;2013:1–11.
24. Bender P, Bogart LK, Posth O, Szczerba W, Rogers SE, Castro A, Nilsson L, Zeng LJ, Sugunan A, Sommertune J and others. Structural and magnetic properties of multi-core nanoparticles analysed using a generalised numerical inversion method. Sci. Reports. 2017;7:1–14.
25. Ristori S, Grillo I, Lusa S, Thamm J, Valentino G, Campani V, Caraglia M, Steiniger F, Luciani P, De Rosa G. Structural characterization of self-assembling hybrid nanoparticles for Bisphosphonate delivery in tumors. Mol Pharm. 2018;15(3):1258–65.

26. He W, Yan J, Sui F, Wang S, Su X, Qu Y, Yang Q, Guo H, Ji M, Lu W and others. Turning a Luffa protein into a self-assembled biodegradable nanoplatform for multitargeted cancer therapy. ACS Nano 2018;12(11):11664–77.
27. Lakshminarayanan R, Ye E, Young DJ, Li Z, Loh XJ. Recent advances in the development of antimicrobial nanoparticles for combating resistant pathogens. Adv Healthc Mat. 2018;7(13):1–13.
28. García I, Henriksen-Lacey M, Calvo J, De Aberasturi DJ, Paz MM, Liz-Marzán LM. Size-dependent transport and cytotoxicity of mitomycin-gold nanoparticle conjugates in 2D and 3D Mammalian cell models. Bioconjugate Chem. 2019;30(1):242–52.
29. de Souza ME, Verdi CM, de Andrade ENC, Santos RCV. Chapter 12—antiviral and antimicrobial (antibacterial) potentiality of nano drugs. In: Mohapatra SS, Ranjan S, Dasgupta N, Mishra RK, Thomas S, editors. Applications of targeted nano drugs and delivery systems. Elsevier; 2019. pp. 327–42.
30. Spagnol C, Fragal EH, Pereira AGB, Nakamura CV, Muniz EC, Follmann HDM, Silva R, Rubira AF. Cellulose nanowhiskers decorated with silver nanoparticles as an additive to antibacterial polymers membranes fabricated by electrospinning. J Coll Interf. Sci. 2018;531:705–15.
31. Cagno V, Andreozzi P, D'Alicarnasso M, Silva PJ, Mueller M, Galloux M, Goffic RL, Jones ST, Vallino M, Hodek J and others. Broad-spectrum non-toxic antiviral nanoparticles with a virucidal inhibition mechanism. Nat Mater. 2018;17(2):195–203.
32. De Souza E, Silva JM, Hanchuk TDM, Santos MI, Kobarg J, Bajgelman MC, Cardoso MB. Viral inhibition mechanism mediated by surface-modified silica nanoparticles. ACS Appl Mater Interf. 2016;8(26):16564–72.
33. Sokolowski M, Bartsch C, Spiering VJ, Prévost S, Appavou MS, Schweins R, Gradzielski M. Preparation of polymer brush grafted anionic or cationic silica nanoparticles: systematic variation of the polymer shell. Macromolecules. 2018;51(17):6936–48.
34. Yi Z, Dumée LF, Garvey CJ, Feng C, She F, Rookes JE, Mudie S, Cahill DM, Kong L. A new insight into growth mechanism and kinetics of mesoporous silica nanoparticles by in situ small angle X-ray scattering. Langmuir. 2015;31(30):8478–87.
35. Wuithschick M, Paul B, Bienert R, Sarfraz A, Vainio U, Sztucki M, Kraehnert R, Strasser P, Rademann K, Emmerling F and others. Size-controlled synthesis of colloidal silver nanoparticles based on mechanistic understanding. Chem Mater. 2013;25(23):4679–89.
36. Varier KM, Gudeppu M, Chinnasamy A, Thangarajan S, Balasubramanian J, Li Y, Gajendran B. Nanoparticles: antimicrobial applications and its prospects. In: Naushad M, Rajendran S, Gracia F, editors. Advanced nanostructured materials for environmental remediation. Cham: Springer International Publishing; 2019. p. 321–55.
37. Lara HH, Ayala-Nuñez NV, Ixtepan-Turrent L, Rodriguez-Padilla C. Mode of antiviral action of silver nanoparticles against HIV-1. J Nanobiotechnol. 2010;8:1–10.
38. Chang ZM, Wang Z, Shao D, Yue J, Xing H, Li L, Ge M, Li M, Yan H, Hu H and others. Shape engineering boosts magnetic mesoporous silica nanoparticle-based isolation and detection of circulating tumor cells. ACS Appl Mater Interf 2018;10(13):10656–63.
39. Singh P, Pandit S, Mokkapati VRSS, Garg A, Ravikumar V, Mijakovic I. Gold nanoparticles in diagnostics and therapeutics for human cancer. Int J Mol Sci 2018;19(7).
40. Sharma A, Goyal AK, Rath G. Recent advances in metal nanoparticles in cancer therapy. J Drug Targ. 2018;26(8):617–32.
41. Dhandapani R, Sethuraman S, Subramanian A. Nanohybrids—cancer theranostics for tiny tumor clusters. J Control Release. 2019;299:21–30.
42. Muhamad N, Plengsuriyakarn T, Na-Bangchang K. Application of active targeting nanoparticle delivery system for chemotherapeutic drugs and traditional/herbal medicines in cancer therapy: a systematic review. Int J Nanomed. 2018;13:3921–35.
43. Le Goas M, Paquirissamy A, Gargouri D, Fadda G, Testard F, Aymes-Chodur C, Jubeli E, Pourcher T, Cambien B, Palacin S and others. Irradiation effects on polymer-grafted gold nanoparticles for cancer therapy. ACS Appl Biomater. 2019;2(1):144–54.
44. Din MI, Arshad F, Hussain Z, Mukhtar M. Green adeptness in the synthesis and stabilization of copper nanoparticles: catalytic, antibacterial, cytotoxicity, and antioxidant activities. Nanoscale Res Lett. 2017;12.

45. Spencer E, Kolesnikov A, Woodfield B, Ross N. New insights about CuO nanoparticles from inelastic neutron scattering. Nanomaterials. 2019;9(3):312.
46. Spinozzi F, Ceccone G, Moretti P, Campanella G, Ferrero C, Combet S, Ojea-Jimenez I, Ghigna P. Structural and thermodynamic properties of nanoparticle-protein complexes: a combined SAXS and SANS study. Langmuir. 2017;33(9):2248–56.
47. Esmaeilzadeh P, Köwitsch A, Liedmann A, Menzel M, Fuhrmann B, Schmidt G, Klehm J, Groth T. Stimuli-responsive multilayers based on thiolated polysaccharides that affect fibroblast cell adhesion. ACS Appl Mater Interf. 2018;10(10):8507–18.
48. Bohn DR, Lobato FO, Thill AS, Steffens L, Raabe M, Donida B, Vargas CR, Moura DJ, Bernardi F, Poletto F. Artificial cerium-based proenzymes confined in lyotropic liquid crystals: synthetic strategy and on-demand activation. J Mater Chem B. 2018;6(30):4920–8.
49. Xu LC, Siedlecki CA. Protein adsorption, platelet adhesion, and bacterial adhesion to polyethylene-glycol-textured polyurethane biomaterial surfaces. J Biomed Mater Res. 2017;105(3):668–78.
50. Christo SN, Bachhuka A, Diener KR, Mierczynska A, Hayball JD, Vasilev K. The role of surface nanotopography and Chemistry on primary neutrophil and macrophage cellular responses. Adv Healthcare Mater. 2016;5(8):956–65.
51. Wang PY, Bennetsen DT, Foss M, Ameringer T, Thissen H, Kingshott P. Modulation of human mesenchymal stem cell behavior on ordered tantalum nanotopographies fabricated using colloidal lithography and glancing angle deposition. ACS Appl Mater Interf. 2015;7(8):4979–89.
52. Batista P, Castro PM, Madureira AR, Sarmento B, Pintado M. Recent insights in the use of nanocarriers for the oral delivery of bioactive proteins and peptides. Peptides. 2018;101:112–23.
53. Li SK, Liu ZT, Li JY, Chen AY, Chai YQ, Yuan R, Zhuo Y. Enzyme-free target recycling and double-output amplification system for electrochemiluminescent assay of Mucin 1 with MoS2 nanoflowers as Co-reaction accelerator. ACS Appl Mat Interf. 2018;10(17):14483–90.
54. Sezen H, Suzer S. XPS for chemical- and charge-sensitive analyses. Thin Solid Films. 2013;534:1–11.
55. Watts JF, Wolstenholme J. Electron spectroscopy: some basic concepts. An introduction to surface analysis by XPS and AES. Chichester, UK: Wiley & Sons, Ltd.; 2003. pp. 1–15.
56. Hofmann S. Introduction and outline. Auger- and X-ray photoelectron spectroscopy in materials science: a user-oriented guide. Berlin, Heidelberg: Springer; 2013. pp. 1–10.
57. Aziz M, Ismail AF. X-ray photoelectron spectroscopy (XPS). Elsevier; 2017. pp. 81–93.
58. Seah MP, Dench WA. Quantitative electron spectroscopy of surfaces: a standard data base for electron inelastic mean free paths in solids. Surf Interf Anal. 1979;1(1):2–11.
59. Fenton OS, Olafson KN, Pillai PS, Mitchell MJ, Langer R. Advances in biomaterials for drug delivery. Adv Mater. 2018;30(29):1–29.
60. Pokhriyal S, Gakkhar N, Bhatia A. Biomedical applications and toxicological effects of nanomaterials: a general approach. J Mat Sci Surf Eng. 2018;6(3):811–6.
61. Sun Y, Fu Y, Luo J, Wang R, Dong Y. Silk fibroin biomaterial-functionalized carbon nanotubes for high water dispersibility and promising biomedical applications. Textile Res J. 2019;89(7):1144–52.
62. Pawlik A, Socha RP, Hubalek Kalbacova M, Sulka GD. Surface modification of nanoporous anodic titanium dioxide layers for drug delivery systems and enhanced SAOS-2 cell response. Coll Surf B. 2018;171:58–66.
63. Lim WS, Chen K, Chong TW, Xiong GM, Birch WR, Pan J, Lee BH, Er PS, Salvekar AV, Venkatraman SS and others. A bilayer swellable drug-eluting ureteric stent: Localized drug delivery to treat Urothelial diseases. Biomaterials 2018;165:25–38.
64. Mitić Ž, Stolić A, Stojanović S, Najman S, Ignjatović N, Nikolić G, Trajanović M. Instrumental methods and techniques for structural and physicochemical characterization of biomaterials and bone tissue: a review. Mater Sci Eng C. 2017;79:930–49.
65. Ajdnik U, Zemljič LF, Bračič M, Maver U, Plohl O, Rebol J. Functionalisation of silicone by drug-embedded chitosan nanoparticles for potential applications in otorhinolaryngology. Materials. 2019;16(6):1–20.

66. He J, Chen J, Hu G, Wang L, Zheng J, Zhan J, Zhu Y, Zhong C, Shi X, Liu S and others. Immobilization of an antimicrobial peptide on silicon surface with stable activity by click chemistry. J Mater Chem B 2017;6(1):68–74.
67. Duta L, Ristoscu C, Stan GE, Husanu MA, Besleaga C, Chifiriuc MC, Lazar V, Bleotu C, Miculescu F, Mihailescu N and others. New bio-active, antimicrobial and adherent coatings of nanostructured carbon double-reinforced with silver and silicon by Matrix-Assisted Pulsed Laser Evaporation for medical applications. Appl Surf Sci. 2018;441:871–83.
68. Chia X, Fojtu M, Masar M. Black Phosphorus nanoparticles potentiate the anticancer effect of Oxaliplatin in ovarian cancer cell line. Adv Funct Mater. 2017;1701955(36):1–7.
69. Todea M, Simon S, Simon V, Eniu D. XPS investigation of new solid forms of 5-fluorouracil with piperazine. J Mol Struct. 2018.
70. Calvin S. XAFS for everyone. Boca Raton: Taylor & Francis Group; 2013. p. 459.
71. Charlet L, Manceau A. Chapter 4: Structure, formation and reactivity of hydrous oxide particles; insights from X-ray absorption spectroscopy. In: Buffle J, van Leeuwen HP, editors. Environmental particles 2. Boca Raton: CRC Press; 1993. p. 118–64.
72. Frenkel AI. Applications of extended X-ray absorption fine-structure spectroscopy to studies of bimetallic nanoparticle catalysts. Chem Soc Rev. 2012;41(24):8163–78.
73. Frenkel AI, Wang Q, Sanchez SI, Small MW, Nuzzo RG. Short range order in bimetallic nanoalloys: an extended X-ray absorption fine structure study. J Chem Phys. 2013;138(6):064202.
74. Faraci G. Cluster characterization by EXAFS spectroscopy. In: AIP 2002; 2002. pp. 173–177.
75. Koningsberger DC, Mojet BL, van Dorssen GE, Ramaker DE. XAFS spectroscopy; fundamental principles and data analysis. Topics Catal. 2000;10(3–4):143–55.
76. Azharuddin M, Zhu GH, Das D, Ozgur E, Uzun L, Turner APF, Patra HK. A repertoire of biomedical applications of noble metal nanoparticles. Chem Comm 2019:6964–96.
77. Kravtsova AN, Guda LV, Polozhentsev OE, Pankin IA, Soldatov AV. Xanes specroscopic diagnostics of the 3D local atomic structure of nanostructured materials. J Struct Chem. 2018;59(7):1691–706.
78. Rubina MS, Said-Galiev EE, Naumkin AV, Shulenina AV, Belyakova OA, Vasil'kov AY. Preparation and characterization of biomedical collagen–chitosan scaffolds with entrapped ibuprofen and silver nanoparticles. Pol Eng Sci. 2019:1–9.
79. Mdlovu NV, Mavuso FA, Lin KS, Chang TW, Chen Y, Wang SSS, Wu CM, Mdlovu NB, Lin YS. Iron oxide-pluronic F127 polymer nanocomposites as carriers for a doxorubicin drug delivery system. Coll Surf A. 2018;2019(562):361–9.
80. Su FX, Zhao X, Dai C, Li YJ, Yang CX, Yan XP. A multifunctional persistent luminescent nanoprobe for imaging guided dual-stimulus responsive and triple-synergistic therapy of drug resistant tumor cells. Chem Comm. 2019;55(36):5283–6.
81. Lima TARM, Valerio MEG. X-ray absorption fine structure spectroscopy and photoluminescence study of multifunctional europium (III)-doped hydroxyapatite in the presence of cationic surfactant medium. J Luminescence 2018;201(Iii):70–76.